

Supporting Information

Phase, Conductivity and Surface Coordination Environment in Two Dimensional Electrochemistry

*Yangye Sun¹, Peiyuan Zhuang², Wei Jiang³, Hu Xu⁴, Simeng Zhang⁴, Ningning Xuan¹, Kun Ba¹, Hanqi Liu¹,
Jianlu Wang³, Wenzhong Bao⁴, Jianfeng Shen^{2*}, Zhengzong Sun^{1*}*

*¹ Department of Chemistry and Shanghai Key Laboratory of Molecular Catalysis and Innovative Materials,
Fudan University, Shanghai 200433, P. R. China;*

² Institute of Special Materials and Technology, Fudan University, Shanghai 200433, P. R. China;

*³ Shanghai Institute of Technical Physics of the Chinese Academy of Sciences, Shanghai 200083, P. R.
China;*

⁴ Institute of Microelectronics, Fudan University, Shanghai 200433, P. R. China.

**Correspondence to: zhengzong_sun@fudan.edu.cn; jfshen@fudan.edu.cn*

Methods

Synthesis of 2H-, 1T'- and 1T-MoTe₂. The three phases of MoTe₂ ultrathin films were synthesized by tellurization of Mo film using chemical vapor deposition. A two-zone tube furnace equipped with mass flow controllers and a vacuum pump was used. Tellurium powder (99.999%) was placed in a ceramic boat in the center of upstream zone. Mo film was deposited on 285 nm SiO₂/Si substrate by e-beam evaporation, and the substrate is placed in the center of downstream zone. The distance between the centers of two temperature zones is 8 cm.

Three phases of MoTe₂ can be obtained by controlling the tellurization degree and growth temperature. When the growth temperature is below 700 °C, 2H- and 1T'- MoTe₂ can be obtained, specifically determined by tellurium vapor pressure(P(Te)) and growth time(t). The phase transforms from 1T' to 2H when we increase P(Te) and t. Mixed 1T'-2H phase occurs in the transitional area in the growth coordination system.

As for 1T-MoTe₂, on the basis of previous computational modeling, high growth temperature is necessary to meet the requirement of its thermodynamic stability. When the reaction temperature is beyond 800 °C, homogeneous 1T-MoTe₂ film can be obtained.

Synthesis of single-layer graphene. 10-μm thick-Cu foils were used as growth substrates. A standard 1-inch tube furnace was used as the CVD chamber. The copper foils were annealed under a hydrogen atmosphere (200 s.c.c.m. hydrogen and ~ 76 torr total pressure) at 1,050 °C for 30 mins prior to the growth. Then 50 s.c.c.m methane and 40 s.c.c.m. H₂ were introduced into the tube to synthesize SLG at 1,050 °C for 30 min.

TEM sample preparation and characterization. The poly (pyromellitic dianhydride-co-4,4'-oxydianiline), amic acid solution (PAA) (15.0-16.0 wt. % in NMP) was dropped onto the MoTe₂/SiO₂/Si and cured on the hot plate at 80 °C for 30 min. The curing makes the PAA fit closely with MoTe₂ ultrathin film. Then the PAA/MoTe₂ was torn off from the SiO₂/Si substrate. We put it on the TEM microgrid support film, with MoTe₂ seating on the grid. The upper PAA was slowly dissolved by NMP and MoTe₂ ultrathin film was left on the grid.

Pristine MoTe₂ electrode preparation process. The indium wire was first pressed on the as-grown MoTe₂/SiO₂/Si samples, with a copper foil binding onto it as the lead. The part of MoTe₂ which contacted with indium wire was inevitably broken during the pressing procedure, leading to both side-contact and plane-contact with the MoTe₂ layer. Then the indium wire, the attached copper foil and the Si substrate were sealed by silica gel to avoid current leakage during the electrochemical measurement. The tail of the copper foil and

a MoTe₂ film catalytic window was exposed. The whole electrode was dried at 25 °C for 3h and then could be used for HER.

MoTe₂/SLG electrodes preparation process. 4% PMMA (alfa Aesar)/anisole solution was spin-coated on the SLG/Cu with the rate of 3000 r/min and dried at 80 °C for 15 min. The spin-coating process was repeated once to ensure the mechanical strength of the PMMA film. Then the copper foil was fast etched in the Marble solution for 2 min and slowly etched in 0.1 M ammonium persulfate aqueous solution for 3 h. The obtained SLG/PMMA film was cleaned in deionized water and fished up by MoTe₂/SiO₂/Si. Then the PMMA/SLG/MoTe₂/SiO₂/Si structure was natural dried for 12 h to get a close joint of SLG and MoTe₂ film. 15% PMMA/anisole solution was spin-coated on the 4% PMMA film with the rate of 1000 r/min and cured at 120 °C for 30min. Then the curing temperature was ramped up to 200 °C and cured for 15min. After that, the whole sample was soaked in HF/NH₄F buffered oxide etchant to etch SiO₂/Si substrate. The exfoliated MoTe₂/SLG/PMMA was cleaned in the deionized water and dried by N₂. A copper foil was linked with the MoTe₂/SLG electrode by the assistance of liquid metal. When the temperature is cooled down to 47 °C, the liquid metal solidified and adhere the copper foil to MoTe₂/SLG/PMMA. Finally, the whole electrode was sealed by the silica gel, with a MoTe₂/SLG window exposed for HER.

Electrochemical characterization. Electrochemical measurements were carried out in a three-electrode system using a CHI 660E electrochemical workstation. Linear sweep voltammetry (LSV) with a 5 mV/s scan rate was performed in 0.5 M H₂SO₄ electrolyte. The reference electrode is the Hg/Hg₂SO₄ electrode and the counter electrode is a graphite paper. The above pristine MoTe₂ electrodes and MoTe₂/SLG electrodes are used as the working electrode. EIS were performed in the same configuration at the overpotential of 0.4 V (vs. RHE) from 1 MHz to 0.1 Hz with an AC voltage of 10 mV.

Lithiation of MoTe₂/SLG electrodes. The lithiation treatment was carried out in a three-electrode system using a CHI 660E electrochemical workstation, with 1 M LiClO₄/ propylene carbonate solution as the electrolyte and two lithium sheets as the reference electrode and the counter electrode, respectively. Chronopotentiometry was performed to realize the lithium intercalation at the potential (vs. Li⁺/Li) from 3.0 V to 0.85 V, with the cathode current of 0.5 μA. When the lithiation was finished, MoTe₂/SLG electrode was dipped in absolute ethyl alcohol for 5 min to remove the lithium. Then the electrode was dried by N₂ and used for electrochemical characterizations.

Focused ion beam (FIB) treatment of MoTe₂/SLG electrodes. The FIB treatment of MoTe₂/SLG electrodes was carried out using FEI Helios NanoLab G4 dual beam. The diameter of each circular hole is 10 μm and the array is rectangular, with 20 holes in length and 10 holes in width.

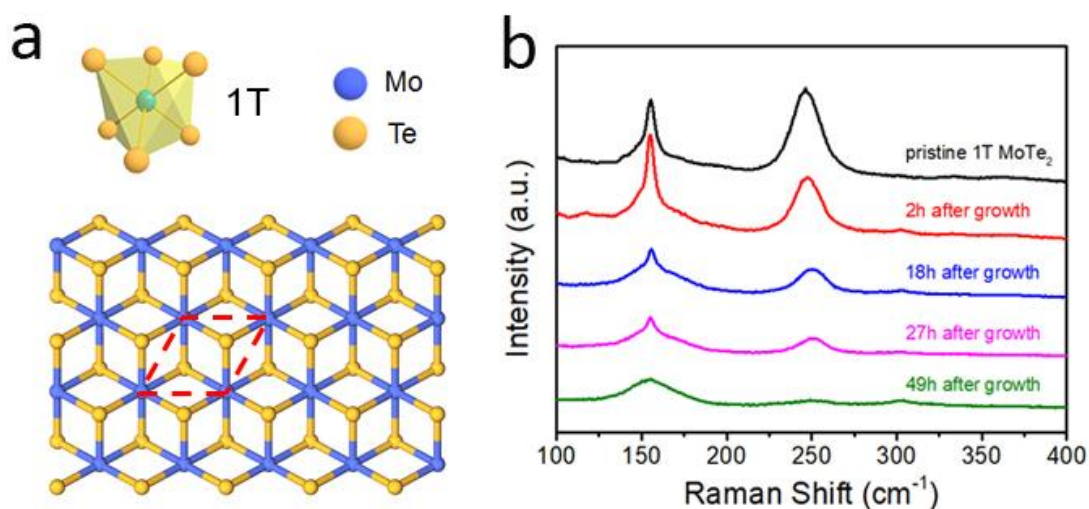


Figure S1: a, Metal coordination and top view structure of 1T-MoTe₂, with unit cell indicated in red dash line. **b**, The evolution of characteristic Raman peaks of 1T-MoTe₂ stored without protection.

18 hours after growth, the intensity of the Raman mode at 249 cm⁻¹ decreases to about one-third of the pristine value. 49 hours after growth, the vibration mode at 249 cm⁻¹ almost disappears, indicating the instability of as-grown 1T-MoTe₂.

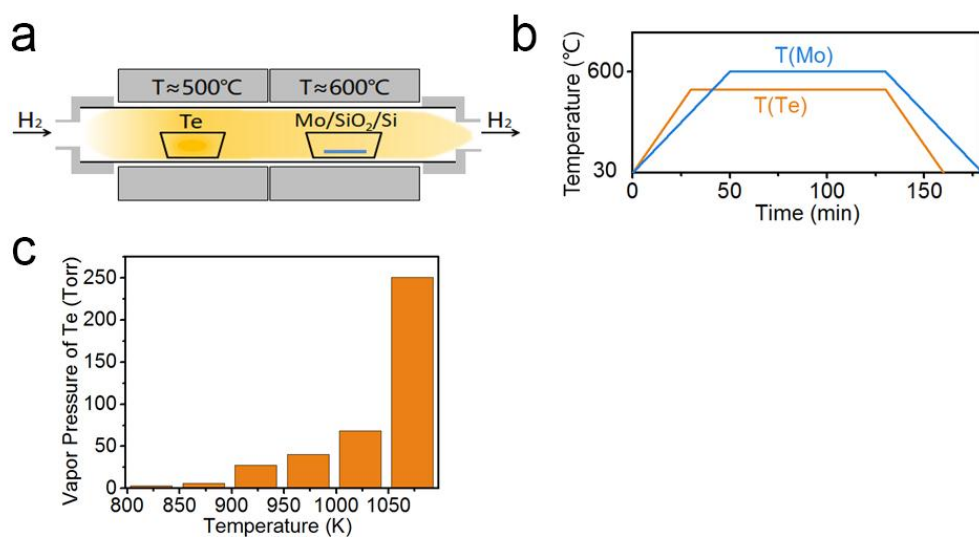


Figure S2: Synthetic details of 2H, 1T' and 1T MoTe₂ ultrathin films. **a**, Schematic diagram of the two-zone CVD system to grow MoTe₂ films. **b**, Temperature evolution of Mo zone(blue) and Te zone(orange), respectively. **c**, Vapor pressure of tellurium under different temperatures ¹.

Table S1. The detailed phase-controlling growth conditions of 2H-, 2H-1T'-, 1T'- and 1T-MoTe₂.

Sample	T(Mo)/°C	P(Te)/Torr	t/min	phase
1	595	5.7	90	2H
2	590	5.5	80	2H
3	630	26.6	90	2H
4	630	26.6	60	2H-1T'
5	590	0.8	80	2H-1T'
6	580	5.3	50	2H-1T'
7	580	5.3	40	2H-1T'
8	700	0.8	5	1T'
9	650	28.1	40	1T'
10	600	7.2	10	1T'
11	600	7.2	3	1T'
12	590	0.1	90	1T'
13	590	0.1	80	1T'
14	500	28.1	20	1T'
15	500	7.2	5	1T'
16	500	0.3	10	1T'
17	500	0.8	5	1T'
18	500	0.8	20	1T'
19	820	0.8	5	1T
20	800	7.2	3	1T
21	800	0.8	3	1T

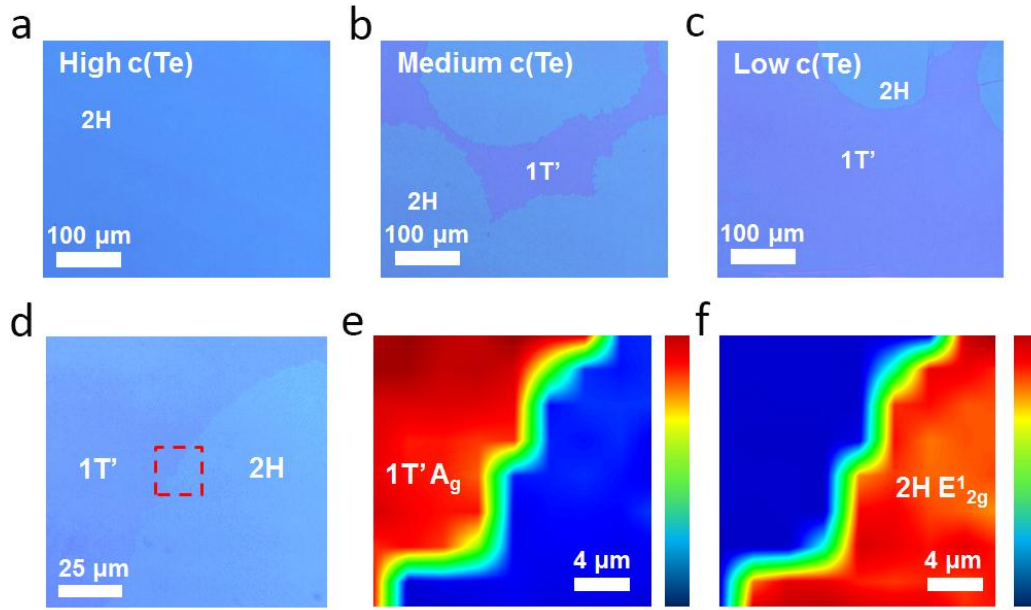


Figure S3: **a-c**, Phase distribution of MoTe₂ film located (a) upstream, (b) midstream, to (c) downstream. The distances between the above a-c samples and tellurium source are 10 cm, 15cm, and 20 cm, respectively. The tellurium concentration decreases as the carrier gas flows and the concentration gradient leads to the phase evolution of MoTe₂ film at different locations. There's an apparent optical contrast between 1T'- and 2H-MoTe₂ film, which can be utilized to distinguish the area of these two phases. **d-f**, The corresponding relationship between optical contrast and phase difference is determined by Raman mapping of the heterojunction area.

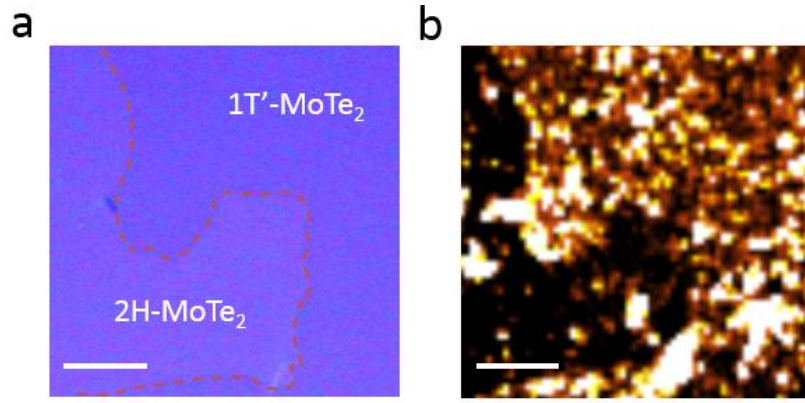


Figure S4: Second harmonics of as-grown 2H/1T'-MoTe₂ heterostructure. **a**, The optical image of the 2H/1T'-MoTe₂ heterostructure, with the phase boundary highlighted by the red dash line. **b**, SHG image of the region shown in (a). The scale bar is 5μm.

For 1T'-MoTe₂, the inversion symmetry is broken for even numbers of layers, leading to a strong SHG signal. However, for 2H-MoTe₂, SHG signal appears with an odd layer number, when lacking the inversion symmetry².

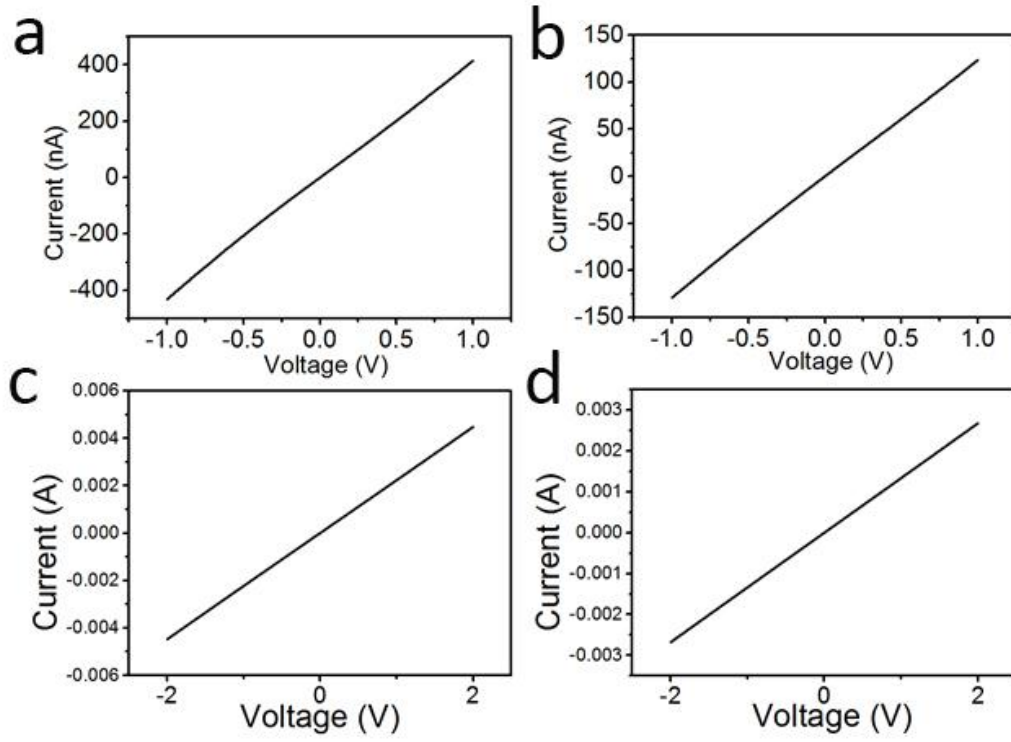


Figure S5: Two-electrode I-V measurement and the intrinsic sheet resistance calculation of 2H- and 1T'-MoTe₂ using transmission line method (TLM). a-b, 2H-MoTe₂ devices with the channel length of 30 μm (a) and 150 μm (b), respectively. c-d, 1T'-MoTe₂ devices with the channel length of 10 μm (c) and 150 μm (d), respectively.

$$R_i \times \frac{L}{W} + 2 \times R_c = \frac{U}{I}$$

Where R_i denotes the sheet resistance (Ω/\square), L denotes the channel length (m), W denotes the channel width (m), R_c denotes the contact resistance (Ω), U denotes the voltage (V) and I denotes the current (A).

For 2H-MoTe₂:

When the channel length is 30 μm,

$$30 \times 10^{-6} \times \frac{R_i}{20 \times 10^{-6}} + 2 \times R_c = \frac{1}{414 \times 10^{-9}}$$

When the channel length is 150 μm,

$$150 \times 10^{-6} \times \frac{R_i}{20 \times 10^{-6}} + 2 \times R_c = \frac{1}{123 \times 10^{-9}}$$

thus $R_i = 0.95 \text{ M}\Omega/\square$; $R_c = 490 \text{ k}\Omega$.

For 1T'-MoTe₂:

When the channel length is 10 μm,

$$10 \times 10^{-6} \times \frac{R_i}{345 \times 10^{-6}} + 2 \times R_c = \frac{2}{4.48 \times 10^{-3}}$$

When the channel length is 20 μm,

$$20 \times 10^{-6} \times \frac{R_i}{345 \times 10^{-6}} + 2 \times R_c = \frac{2}{2.68 \times 10^{-3}}$$

thus $R_i = 10.35 \text{ k}\Omega/\square$; $R_c = 73.2 \text{ }\Omega$.

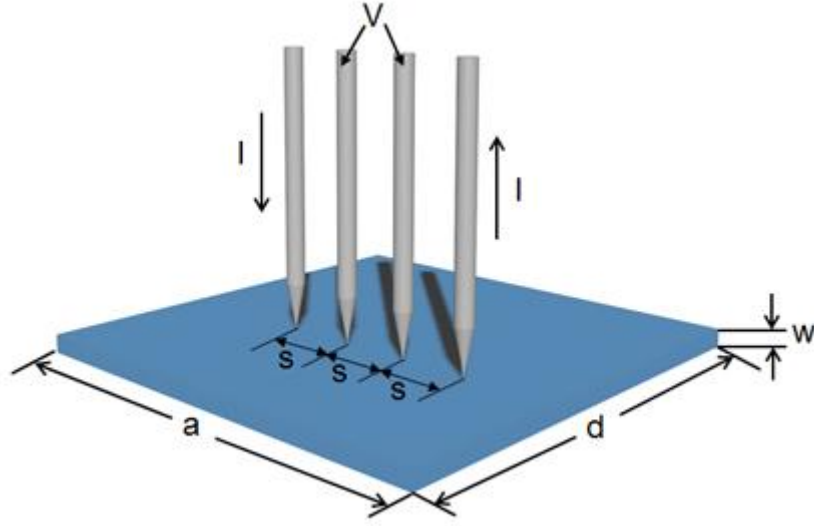


Figure S6: Arrangement of sheet resistance measurement on SLG and MoTe₂ samples.

The sheet resistance is calculated by a previous reported method³. The related equations are displayed below:

$$R_{\square} = \frac{\rho}{w}$$

$$\rho = C \times \frac{V}{I} \times G\left(\frac{w}{s}\right) \times D\left(\frac{d}{s}\right)$$

$$C = 2 \times \pi \times s$$

where I denotes the current, V denotes the voltage and ρ denotes the resistivity. $G\left(\frac{w}{s}\right)$, $D\left(\frac{d}{s}\right)$ are correction factors determined by: sheet thickness (w), sheet length (d), sheet width (a) and probe distance (s). Here $s=1$ mm, $a = 10$ mm, $d = 10$ mm, $w = 0.3$ nm for SLG and 5.0 nm for MoTe₂.

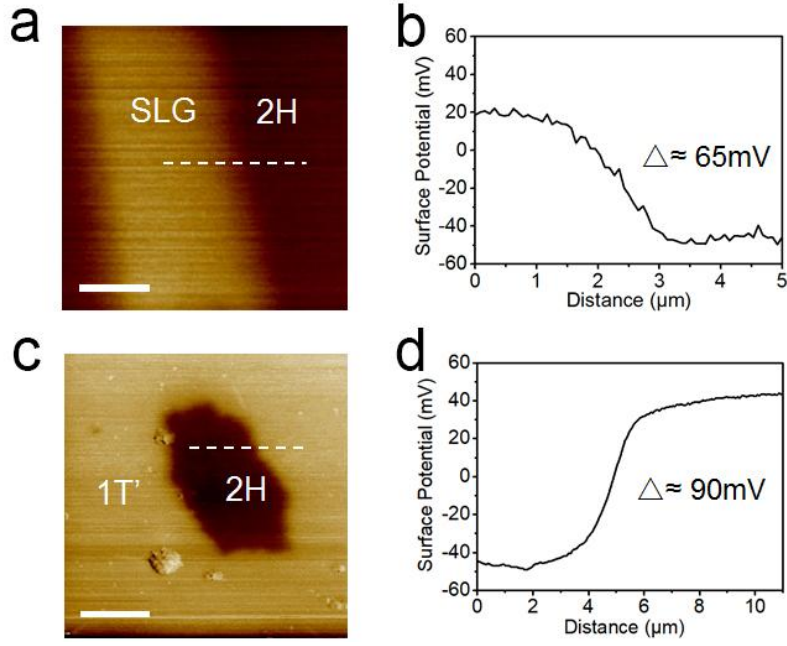


Figure S7: Surface potential measurement of 2H-/1T'-MoTe₂ heterostructure. **a**, The surface potential image of 2H-MoTe₂/SLG heterostructure (scale bar: 2μm). **b**, The surface potential profile for the chosen area (white dashed line in (a)). **c**, The surface potential image of 2H-/1T'-MoTe₂ heterostructure (scale bar: 5μm). **d**, The surface potential profile for the chosen area (white dashed line in (c)).

Suppose the ‘contact potential difference’ as CPD, the work function of 2H-MoTe₂, 1T'-MoTe₂ and SLG are ϕ_{2H} , $\phi_{1T'}$ and ϕ_{SLG} , separately.

By carefully adjusting external bias V_{CPD} , a compensatory potential, to nullify the electric field resulting from the Fermi energy level difference, we can get the CPD and all surface charges, which is equal to the applied bias⁴.

$$\phi_{2H} = \phi_{SLG} - e \times V_{CPD}$$

where $\phi_{SLG} = 4.55 \pm 0.02$ eV⁵, $V_{CPD} \approx -0.065$ V.

Then ϕ_{2H} is determined as 4.615 ± 0.02 eV.

Then the work function of 2H-MoTe₂ is determined as ~ 4.59 V:

$$\phi_{2H} = \phi_{1T'} - e \times V_{CPD}$$

$V_{CPD} \approx -0.09$ V, then $\phi_{1T'}$ is determined to be 4.525 ± 0.02 eV, in accord with the theoretical value of ~ 4.50 eV⁵.

Therefore, 2H- and 1T'-MoTe₂ both show excellent work function alignment with the SLG substrate, with tiny differences of about 0.020 eV and 0.065 V, respectively.

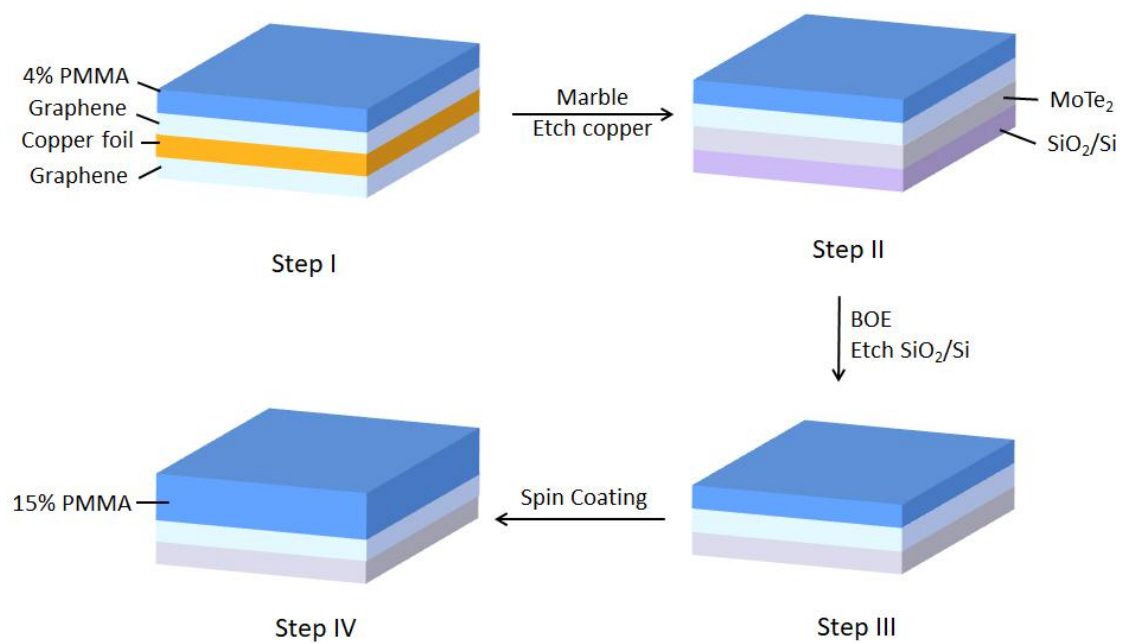


Figure S8: Schematic diagram of MoTe₂/SLG electrode preparation process.

Table S2. Fresh-prepared 2H-, 1T'-, and 1T-MoTe₂'s sheet resistance measured by transmission line method* and four-probe method.**

Phase	2H	1T'	1T
		10.35*	
Sheet Resistance(k Ω /□)	950*	4.3(\pm 0.3)**	20.3(\pm 1.9)**

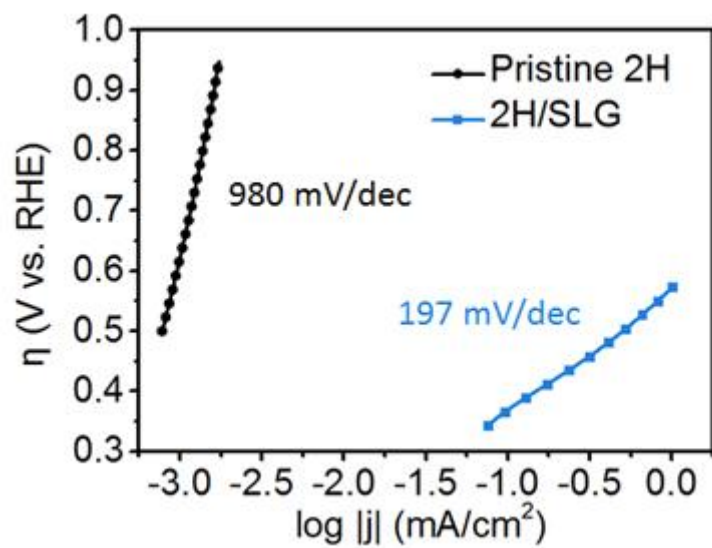


Figure S9: Tafel slopes of the pristine 2H-MoTe₂ and 2H-MoTe₂/SLG electrodes.

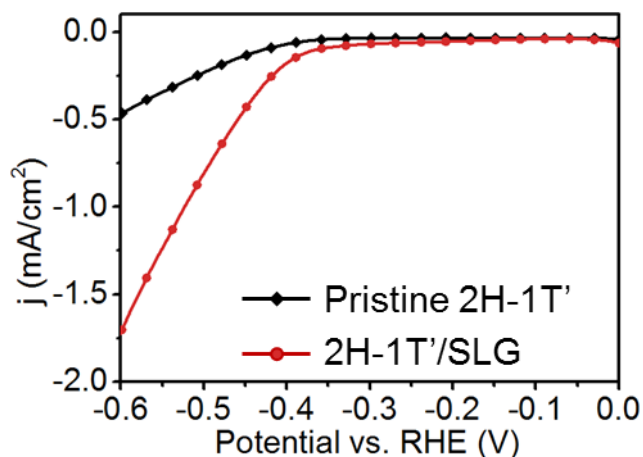


Figure S10: The HER performance of pristine 2H-1T' MoTe₂ (black) and 2H-1T' MoTe₂/SLG (red) sample.

The coverages of 2H-phase islands in both samples are ~40%, with 1T'-phase surrounded. For pristine phase mixture sample, the current density is 0.47 mA/cm² when the overpotential is - 0.6V (vs. RHE), smaller than the value of 2.8 mA/cm² for pristine 1T'-MoTe₂. The performance degradation is originated from both the poor conductivity of pristine semiconducting 2H-phase and its current hinder effect towards 1T'-phase. However, the 2H-1T' MoTe₂/SLG sample shows a much better performance, with a current density of 1.7 mA/cm² ($\eta = -0.6\text{V}$ vs. RHE), comparable to that of pure 2H-MoTe₂/SLG electrode. This further proves that the electron propagation becomes more efficient due to the assistance of SLG and the perpendicular tunneling pathway.

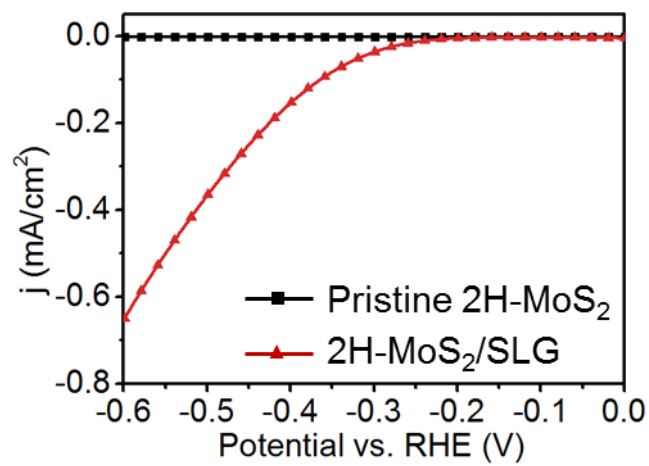


Figure S11: The HER performance of pristine 2H-MoS₂ film and 2H-MoS₂/SLG electrode.

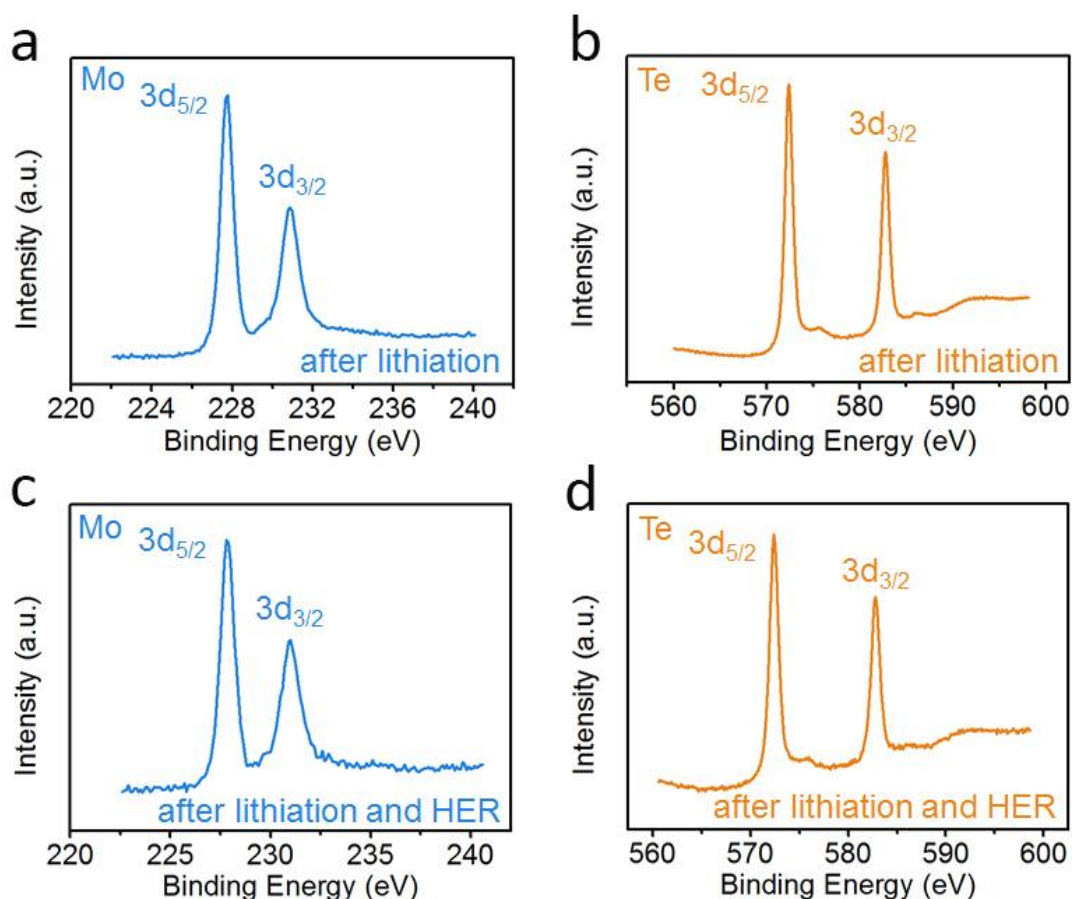


Figure S12: XPS analysis of 2H-MoTe₂/SLG electrode after lithiation treatment. **a-b**, 2H-MoTe₂ after lithiation shows similar chemical environment with that of before lithiation. **c-d**, After lithiation and the following HER, the surface coordination environment of 2H-MoTe₂ still remains the same.

The above results indicate that 2H-MoTe₂ film has high surface stability and can endure the electrode fabricating process, the lithium intercalation and the HER process, with no obvious oxide or other signals being found.

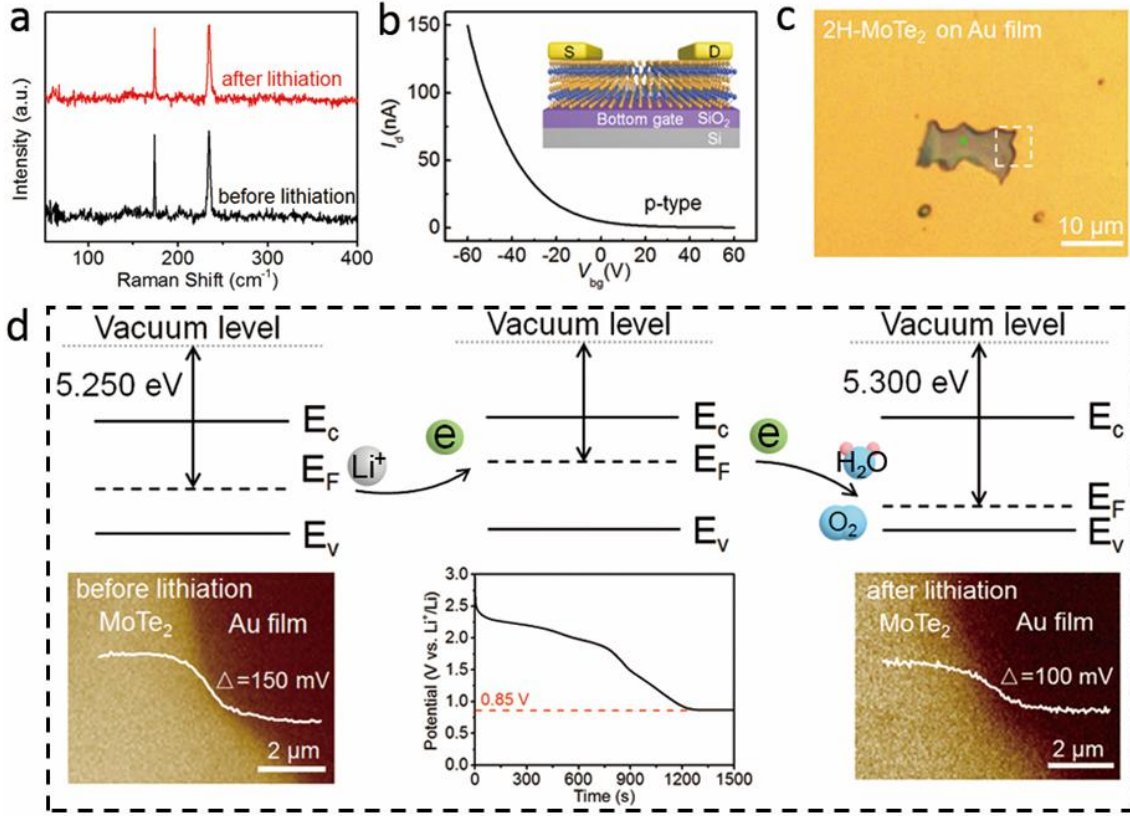


Figure S13: Surface potential and work function evolution of 2H-MoTe₂ before and after the lithium treatment. **a**, The Raman spectra of 2H-MoTe₂ before and after lithiation. **b**, Transfer characteristics of chemical vapor deposited 5 nm 2H-MoTe₂ film. **c**, The optical image of 2H-MoTe₂ mechanically exfoliated onto the Au film. The dashed line area is where surface potential measurement is carried out. **d**, Band diagram scheme of the lithium ion treatment on 2H-MoTe₂. The work function of pristine 2H-MoTe₂ is calculated to be 5.250 eV, with ~ 150 mV of surface potential (SP) higher than the Au reference (left). Due to the electron donation from Li during lithium intercalation process, the Fermi level of 2H-MoTe₂ moves upward (middle). Then the p-doping effect is reached after exposing the device to air, and electrons are transferred from MoTe₂ to the adsorbed O₂/H₂O, resulting in a ~50 mV decrease in SP and a work function enhancement to 5.300 eV (right).

Since the lithium insertion into gold happens at the potential of 0.2 to 0 V (vs. Li^{+/}Li)⁶, which is far below our lithium intercalation potential range of 3 V to 0.8 V, the gold film is a stable reference during the lithiation process, with a standard work function value of 5.40 eV⁷.

$$\varphi_{2H} = \varphi_{Au} - e \times V_{CPD}$$

Before lithiation (Fig. S13d, left), V_{CPD} = 0.150 V, φ_{2H} = 5.250 eV.

After lithiation (Fig. S13d, right), V_{CPD} = 0.100 V, φ_{2H} = 5.300 eV.

It should be noted that the work function of 2H-MoTe₂ calculated above is higher than that in Figure S6, which is caused by the different work functions of the SLG and Au film references.

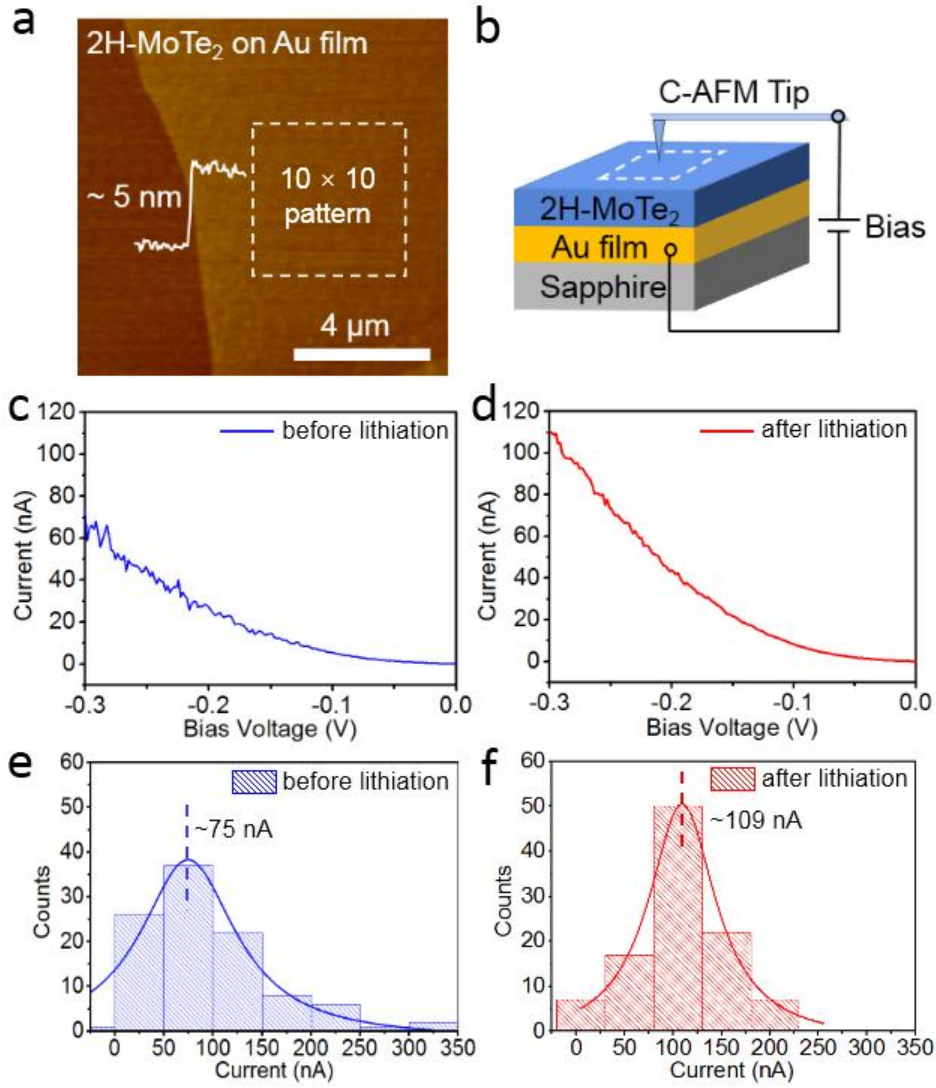


Figure S14: Surface morphology and conductivity analysis of 2H-MoTe₂ before and after lithiation. **a**, AFM of a 2H-MoTe₂ flake and the area selected to do C-AFM before and after the lithiation treatment. **b**, The scheme of the C-AFM setup. **c-d**, The typical I-V curves measured with C-AFM in the selected area before and after lithiation, respectively. **e-f**, Current distributions of 100 sampling points and the corresponding distribution curves fitted by Lorentz function before and after lithiation, respectively.

A 2H-MoTe₂ flake (~ 5 nm thick) is mechanically exfoliated onto an Au-coated substrate. The C-AFM measurement covered a selected area (4.5 μm×4.5 μm) with a 0.5 μm step along both x- and y-axis. The current distribution shows an upshift of ~ 34 nA after the lithiation treatment when the bias voltage on 2H-MoTe₂ is set at -0.3V, indicating the vertical conductivity enhancement for lithiation treated 2H-MoTe₂.

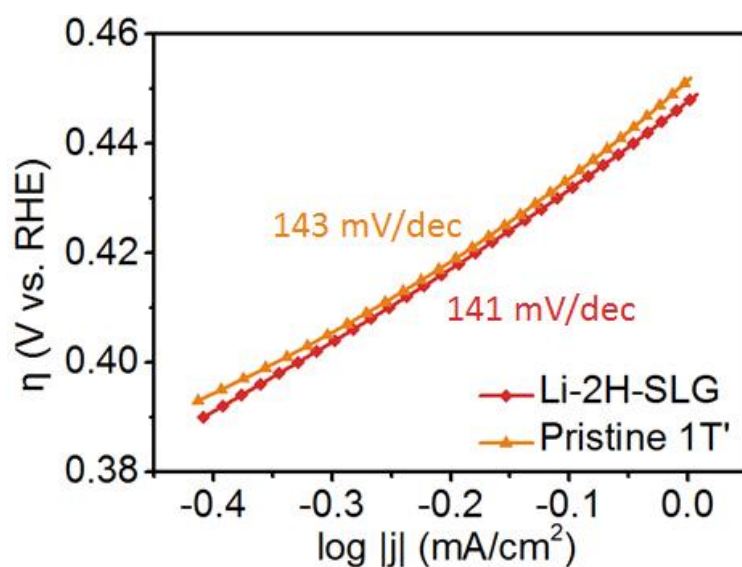


Figure S15: Tafel plots comparison of HER performance between pristine 1T'-MoTe₂(orange) and 2H-MoTe₂/SLG electrode after lithiation(red).

The Tafel slope after lithiation decreases to 141 mV/dec, which is comparable with that of pristine 1T'-MoTe₂ electrode (143 mV/dec).

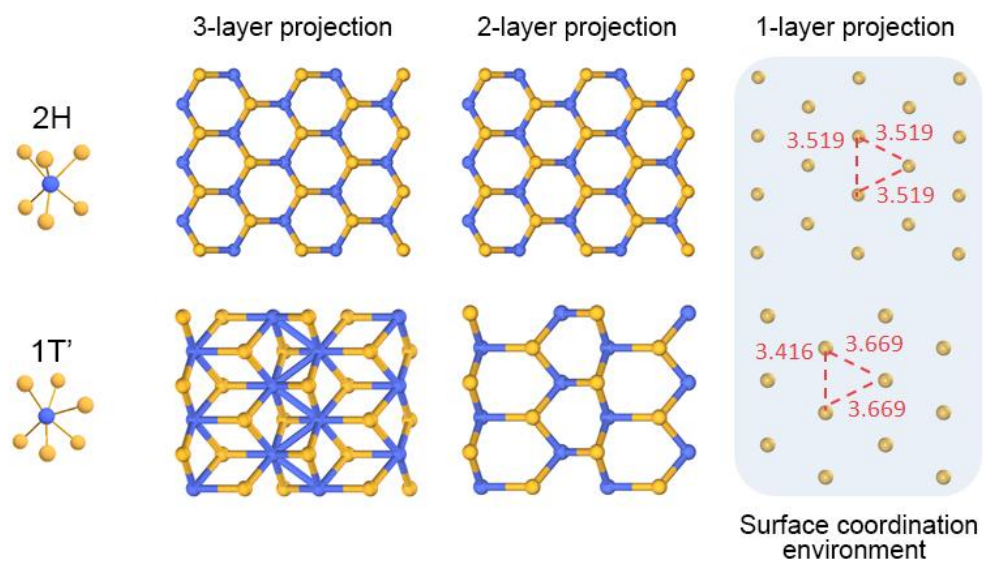


Figure S16: Top view of single layer MoTe₂, with 3-layer, 2-layer and 1-layer atoms projection.

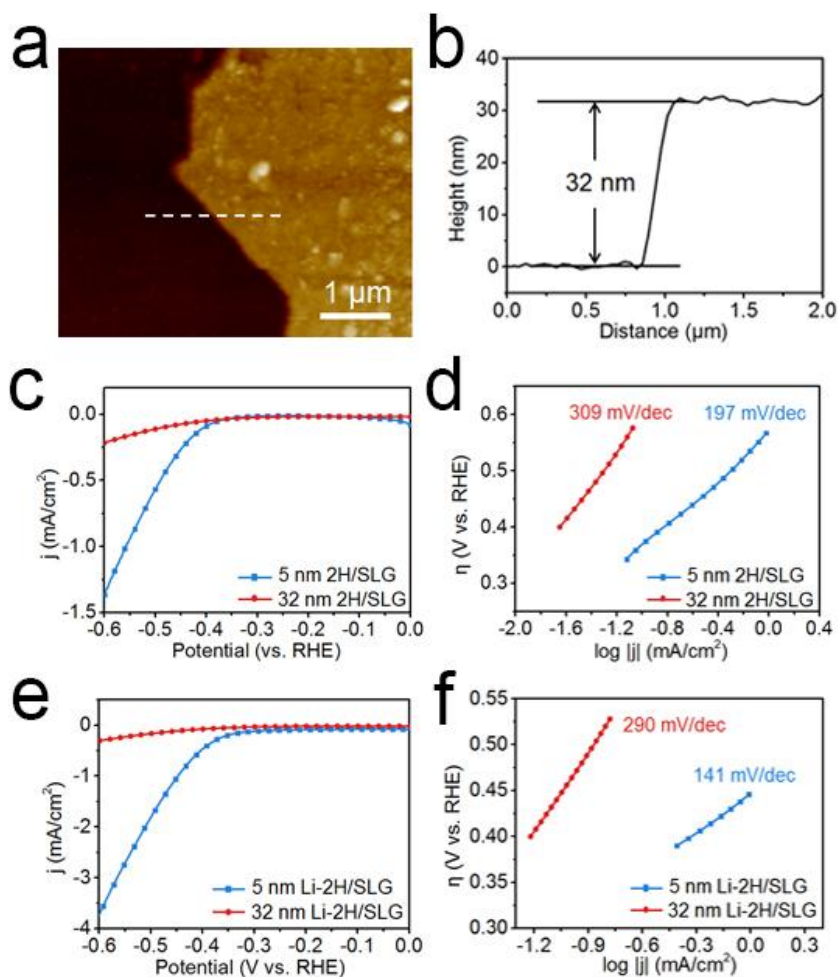


Figure S17: Thickness effect on the extrinsic and intrinsic conductivity engineering. **a-b**, Height image and profile of a 32 nm-thick 2H-MoTe₂ film. **c-d**, The electrocatalytic ability comparison on extrinsic conductivity engineering between ultrathin (5 nm) and thick (32 nm) 2H-MoTe₂ films. **e-f**, The electrocatalytic ability comparison on intrinsic conductivity engineering between ultrathin (5 nm) and thick (32 nm) 2H-MoTe₂ films.

The extrinsic and intrinsic enhancements in HER performance of 32 nm 2H-MoTe₂ are both significantly lower than that of 5 nm 2H-MoTe₂, indicating that the effective extrinsic and intrinsic conductivity promotion are limited in electrocatalytic materials less than 10 layers.

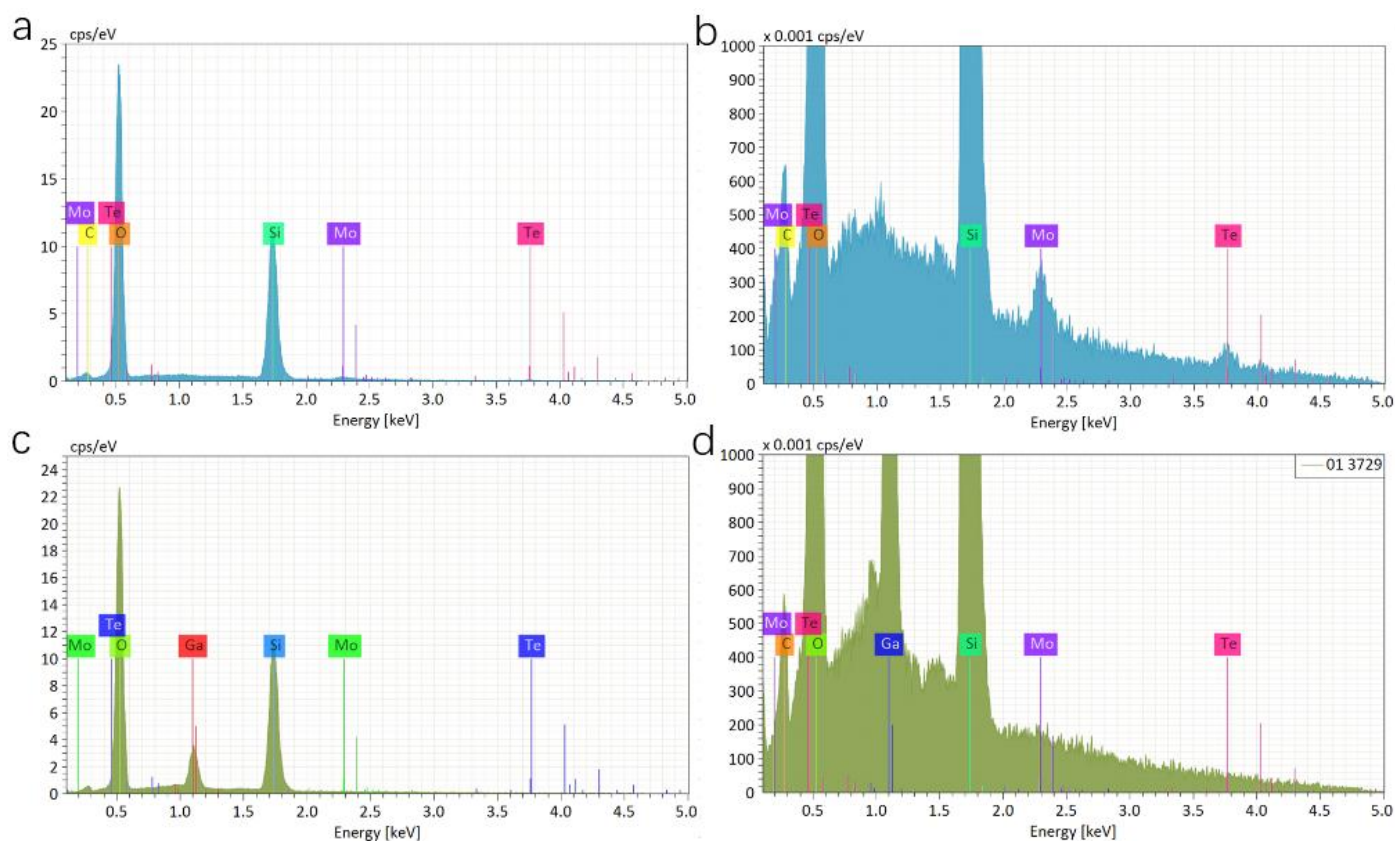


Figure S18: Energy Dispersive Spectra (EDS) analysis of FIB carved 2H-MoTe₂/SLG electrode. a-b, Element distributions at 2H-MoTe₂ basal plane region, with the appearance of Mo and Te. **c-d,** Element distributions at FIB carved region, indicating the thorough cutting of 2H-MoTe₂.

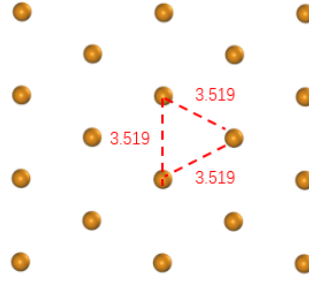


Figure S19: Edge length/ basal plane area ratio and edge/basal plane atomic ratio for FIB carved 2H-MoTe₂/SLG film.

(1) edge length/ basal plane area ratio L_{edge}/S_{plane}

The diameter of the circular hole is 10 μm , and the hole number is 200 (10 \times 20 pattern). The MoTe₂ film has 7 layers. The exposed basal plane area is $6.43 \times 10^{-8} \text{ m}^2$.

$$\frac{L_{edge}}{S_{plane}} = \frac{2 \times \pi \times (5 \times 10^{-6}) \times 200 \times 7}{6.43 \times 10^{-8}} = 6.84 \times 10^5 \text{ m/m}^2$$

(2) edge/basal plane atomic ratio N_{edge}/N_{plane}

The area within the red dashed line is

$$0.5 \times \frac{3^{1/2}}{2} \times (3.519 \times 10^{-10})^2 = 5.36 \times 10^{-20} \text{ m}^2$$

Then there are $3 \times 1/6 = 0.5$ Te atom and $3 \times 1/6 \times 1/2 = 0.25$ Mo atom per $5.36 \times 10^{-20} \text{ m}^2$.

The plane area is $6.43 \times 10^{-8} \text{ m}^2$, so the atom number on the exposed basal plane (N_{plane}) is

$$6.43 \times 10^{-8} \times \frac{0.5 + 0.25}{5.36 \times 10^{-20}} = 8.99 \times 10^{11}$$

$$L_{edge} = 2 \times \pi \times (5 \times 10^{-6}) \times 200 \times 7 = 4.40 \times 10^{-2} \text{ m}$$

The Te atom number at the edge can be estimated as

$$\frac{4.40 \times 10^{-2}}{3.52 \times 10^{-10}} \times 2 = 2.50 \times 10^8$$

Since both Mo and Te atoms are exposed, the number of edge atoms should be multiplied by 1.5 times, so

$$N_{edge} = 3.750 \times 10^8.$$

$$\frac{N_{edge}}{N_{plane}} = \frac{3.75 \times 10^8}{8.99 \times 10^{11}} = 4.17 \times 10^{-4}$$

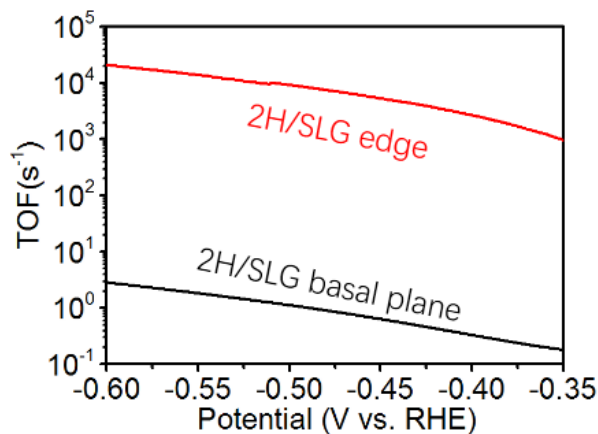


Figure S20: TOF evolution with the applied overpotential for the basal plane and edge atoms of 2H-MoTe₂.

TOF calculation for basal plane atom and edge atom of 2H-MoTe₂⁶.

$$j(\eta) = S \times \text{TOF}(\eta) \times \frac{n \times F}{A \times NA}$$

where $j(\eta)$ is the current density, S is the active site density, n is the number of electrons transferred per product molecule, F is the Faraday constant, A is the exposed electrode area, and NA is Avogadro's number.

Thus,

$$\text{TOF}(\eta) = \frac{j(\eta) \times A \times NA}{S \times n \times F}$$

For 2H-MoTe₂/SLG without FIB:

$$\begin{aligned} \text{TOF}_{\text{basal plane}} &= \frac{j(\eta) \times A \times NA}{S \times n \times F} = \frac{1 \text{ cm}^2 \times 6.022 \times 10^{23} \text{ mol}^{-1}}{1.40 \times 10^{15} \times 2 \times 96485 \text{ C} \cdot \text{mol}^{-1}} \times j(\eta) \\ &= 2229.06 \text{ cm}^2 \text{ C}^{-1} j(\eta) \end{aligned}$$

For 2H-MoTe₂/SLG with FIB:

$$j_{\text{edge}} + j_{\text{basal plane}} = j_{\text{total}}$$

$$(S_{\text{edge}} \times \text{TOF}_{\text{edge}} + S_{\text{basal plane}} \times \text{TOF}_{\text{basal plane}}) \times \frac{n \times F}{A \times NA} = j_{\text{total}}$$

In the above equation, S_{edge} is 3.75×10^8 , $S_{\text{basal plane}}$ is 8.99×10^{11} , A is $6.43 \times 10^{-4} \text{ cm}^2$.

Then the TOF~ η function can be plotted above.

Table S3. Sheet resistance of 2H-MoTe₂/SLG electrode before and after lithiation treatment.

	2H/SLG before lithiation	2H/SLG after lithiation
Sheet Resistance(k Ω /□)	0.8-1.0	0.6

Table S4. The electrocatalytic performance summary of MoTe₂ with different phases, conductivity and surface coordination environments.

	Current Density/(mA/cm ²) (Overpotential = 0.6V vs. RHE)		Tafel (mV/dec)		EIS (Ω ·cm ²)	
	2H	1T'	2H	1T'	2H	1T'
Pristine MoTe ₂	9.6×10 ⁻⁴	2.8	980	143	6×10 ⁵	250
MoTe ₂ /SLG	1.3	2.0	197	130	900	300
Lithiation	3.7	—	141	—	300	—
FIB	5.2	—	108	—	100	—
FIB and lithiation	11.2	—	82	—	30	—

REFERENCES

1. Honig, R. E.; Kramer, D. A. Vapor Pressure Data for the Solid and Liquid Elements. *RCA Rev.* **1969**, *30*, 285-305.
2. Beams, R.; Cancado, L. G.; Krylyuk, S.; Kalish, I.; Kalanyan, B.; Singh, A. K.; Choudhary, K.; Bruma, A.; Vora, P. M.; Tavazza, F.; Davydov, A. V.; Stranick, S. J. Characterization of Few-Layer 1T' MoTe₂ by Polarization-Resolved Second Harmonic Generation and Raman Scattering. *ACS Nano* **2016**, *10*, 9626–9636.
3. Smits, F. M. Measurement of Sheet Resistivities with the Four-point Probe. *The bell system technical journal* **1958**, *20*, 711.
4. Luo, D.; Sun, H.; Li, Y. Kelvin Probe Force Microscopy in Nanoscience and Nanotechnology. In: Kumar C.S.S.R. (eds), *Surface Science Tools for Nanomaterials Characterization*, Springer, Berlin, Heidelberg, **2015**, 117-158.
5. Panchal, V.; Pearce, R.; Yakimova, R.; Tzalenchuk, A.; Kazakova, O. Standardization of Surface Potential Measurements of Graphene Domains. *Sci. Rep.* **2013**, *3*, 2597.
6. Kuilova, T. L. A Study of Lithium Insertion into Electrodes with Thin Gold Films. *Russian J. Electrochem.* **2010**, *46*, 934-938.
7. Uda, M.; Nakamura, A.; Yamamoto, T.; Fujimoto, Y. Work Function of Polycrystalline Ag, Au and Al. *J. Electron Spectrosc. Relat. Phenom.* **1998**, *88-91*, 643-648.